Sensors & Actuators: B. Chemical 348 (2021) 130704

Contents lists available at ScienceDirect

Sensors and Actuators: B. Chemical

journal homepage: www.elsevier.com/locate/snb

H_2 detection mechanism in chemoresistive sensor based on low-cost synthesized WO_3 nanorods

G. Mineo [a,b], K. Moulaee [c], G. Neri [c], S. Mirabella [a,b,*], E. Bruno [a,b]

[a] Dipartimento di Fisica e Astronomia "Ettore Majorana", Università degli Studi di Catania, via S. Sofia 64, 95123 Catania, Italy
[b] CNR-IMM, Università di Catania, via S. Sofia 64, 95123 Catania, Italy
[c] Dipartimento di Ingegneria, Università degli Studi di Messina, Contrada Di Dio, 98158 Sant'Agata, Messina, Italy

ARTICLE INFO

Keywords:
Tungsten-trioxide
Hydrothermal
Nanostructures
Gas sensor
Hydrogen sensing

ABSTRACT

Nanostructured WO_3 represents a promising material for fast and reliable molecular hydrogen detection through chemo-resistive effect. Here, an extended experimental investigation of WO_3-H_2 interaction is presented and modeled. A powder of WO_3 nanorods (400 nm long, 50 nm large) is produced by hydrothermal technique and drop casted on Pt interdigitated electrode. H_2 sensing tests at different concentrations (2000–50,000 ppm) and temperatures (250–400 °C) are reported. Scanning Electron Microscopy (SEM), X-ray Diffraction analysis (XRD), and electrical measurements were performed. The response and recovery kinetics of H_2 sensing are carefully described by using a two-isotherms Langmuir model, and kinetics barriers for WO_3-H_2 interaction are evaluated. Two microscopic processes lead to gas detection. A fast process (shorter than 4 s) is attributed to H_2 interaction with adsorbed oxygen at WO_3 nanorods surface. A slow process (20–1000 s), with activation energy of 0.46 eV, is attributed to oxygen vacancy generation in WO_3. H intercalation in WO_3 is ruled out. The recovery of WO_3 after H_2 exposure is also modeled. The chemo-resistive effect leading to H_2 sensing by WO_3 is explained through the above processes, whose kinetic barriers have been quantified. These data open the route for the development of fast, sensitive, and low-temperature operating H_2 sensors based on WO_3.

1. Introduction

In recent years the scientific community is devoting a large interest to hydrogen as a source of energy, since it is an excellent candidate to replace fossil fuels for many applications, such as chemical industry, power generation, medical treatment, and many others [1–3]. Soon, hydrogen production, transportation, and storage will become key issues for sustainable development. However, H_2 is a colorless, tasteless, and odorless gas which becomes inflammable and explosive when the concentration exceeds 4%. Therefore, fast and very sensitive sensors are necessary where H_2 is produced, stored, and transported to promptly find any leakage. Typically, fast H_2 sensors work at high temperatures (250–400 °C), increasing the explosion danger [4,5]. The progress in H_2 application cannot proceed without a parallel development of safe, fast, and reliable H_2 sensors. To this aim, a proper investigation is needed to unveil the interaction between H_2 and the sensing material leading to reliable detection.

One of the most promising materials for H_2 sensing is WO_3, an *n*-type metal oxide semiconductor with an indirect bandgap ranging between 2.6 and 3.2 eV [6]. It has been widely studied for its reversible chromogenic ability under external stimuli such as electrical bias (electrochromism) or reducing ambient (gaschromism) [7], for its ability to detect many gases such H_2S, NH_3, NO_2, and H_2 [8–11] and for its properties in electrochemical storage application [12,13]. Nanostructured WO_3 shows better performances thanks to a larger surface-to-volume ratio, higher specific surface area, and crystal faceting with marked surface reactivity [14–16]. Further, improvement of performances is obtained by surface decoration with noble monometallic, or bimetallic nanoparticles, such as Pt [17], Pd [18], Au [19] or proper combination of these [20,21] leading to synergistic effects [22].

The affinity of WO_3 for reducing gases makes it an excellent candidate for optical and chemoresistive H_2 sensor realization since low concentrations can be detected also below 250 °C. Zhang et al. [11] synthesized urchin-like hexagonal WO_3 and tested them at 250 °C for H_2 sensing at concentrations ranging between 10 and 80 ppm. Wu et al. [18] synthesized Pd loaded mesoporous WO_3 for H_2 sensing test. They compared bare WO_3, mesoporous WO_3, and Pd-loaded mesoporous WO_3, showing that the latter is the best one in terms of response

* Corresponding author at: Dipartimento di Fisica e Astronomia "Ettore Majorana", Università degli Studi di Catania, via S. Sofia 64, 95123 Catania, Italy.
E-mail address: salvo.mirabella@dfa.unict.it (S. Mirabella).

https://doi.org/10.1016/j.snb.2021.130704
Received 25 June 2021; Received in revised form 24 August 2021; Accepted 31 August 2021
Available online 3 September 2021

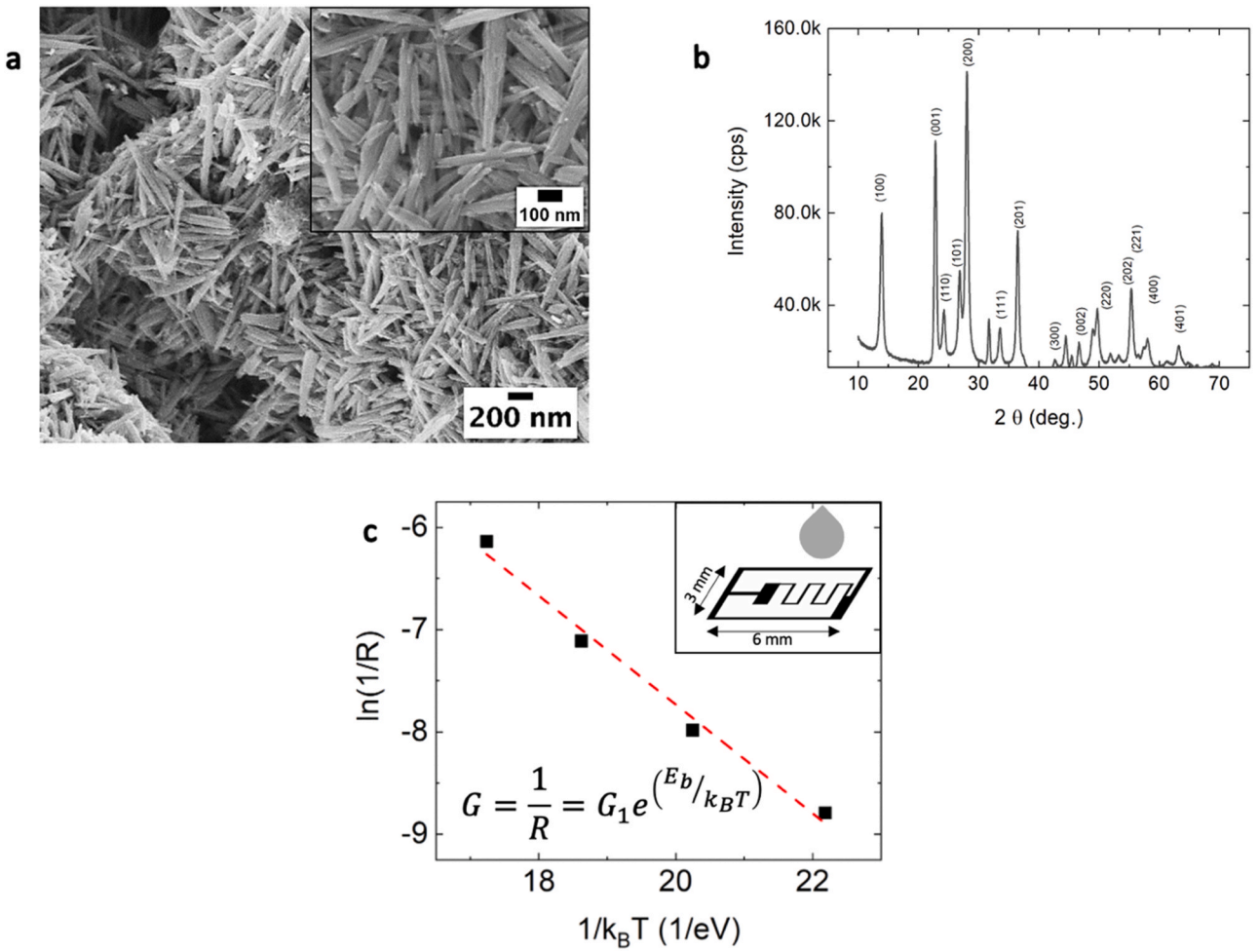

Fig. 1. (a) low and (inset) high magnification SEM image of WO_3 nanorods deposited on the interdigitated substrate, (b) XRD pattern, and (c) Arrhenius plot of inverse of measured resistance (R); inset in (c): schematic of interdigitated substrate drop coated.

efficiency at room temperature at 5000 ppm of H_2. Chang et al. [23] studied the gas sensing performances of Pt-loaded WO_3 thin-film at 200 °C under different concentrations of H_2 (between 1 and 10,000 ppm). Mattoni et al. [17] synthesized a single-crystal Pt-decorated WO_3 thin film and tested it at room temperature under sub-ppm concentration of hydrogen. In 2017, using a density functional theory approach, Tian et al. [24] proposed a model for the interaction between H_2 and hexagonal WO_3, according to which the H_2 sensing mechanism proceeds through H_2O molecules formation after interaction of H_2 with oxygen ions adsorbed onto noble metal nanoparticles, if any. Experimental works by Wu and Chang claimed Tian's model. On the other hand, Mattoni et al. proposed a different model based on adsorption of H_2 on Pt nanoparticles, H_2 dissociation and intercalation of H^+ ions inside the lattice of WO_3. A comprehensive understanding of WO_3-H_2 interaction is still missing, univocal experimental evidence of chemical reactions or energy barriers do not result from literature and a detailed description of temperature-activated kinetics is however required. A basic comprehension of actual processes underlying the WO_3-H_2 interaction could promote a step forward in H_2 sensing by WO_3.

In this paper, we synthesized by hydrothermal technique hexagonal WO_3 nanorods, and we studied the interaction with H_2 molecules at different temperatures and concentrations. The experimental kinetic curves of the material response and recovery were satisfactorily modeled by using two thermally activated processes leading to chemoresistive effect. A comprehensive description of the WO_3-H_2 interaction is discussed.

2. Material and methods

2.1. Synthesis

Hydrothermal synthesis of hexagonal WO_3 nanorods is employed by using sodium tungstate (Na_2WO_4), sodium chloride (NaCl), and HCl [25]. The experimental procedure is detailed here: 0.825 g of Na_2WO_4 is added to 19 ml of deionized water. After stirring for 10 min, a certain quantity of HCl is added to solution to get a 2.4 pH. The solution is then put in a stainless-steel autoclave (25 ml). Before closing, 0.5 g of NaCl is added as a capping agent which leads to hexagonal nanorods morphology [26]. The sealed autoclave is put in an oven at 180 °C for 3 h. The autoclave is cooled down naturally, the obtained powder is separated (by centrifugation at 6000 rpm for 10 min) and washed with water and ethanol several times, finally dried on a hot plate for 1 h.

For the electrode realization, WO_3 nanorods powder is dissolved in 5 ml of deionized water and sonicated for 20 min. Several drops are then dipped on an interdigitated Pt electrode until all the fingers are fully coated.

2.2. Characterization

The morphological analyses were carried out by a scanning electron microscope (SEM) Gemini Field Emission SEM Carl Zeiss SUPRATM 25 (FEG-SEM, Carl Zeiss Microscopy GmbH, Jena, Germany). X-ray diffraction (XRD) patterns were acquired through a Bruker-AXSD5005θ-θdiffractometer, using a Göbel mirror to parallel the Cu Kα radiation

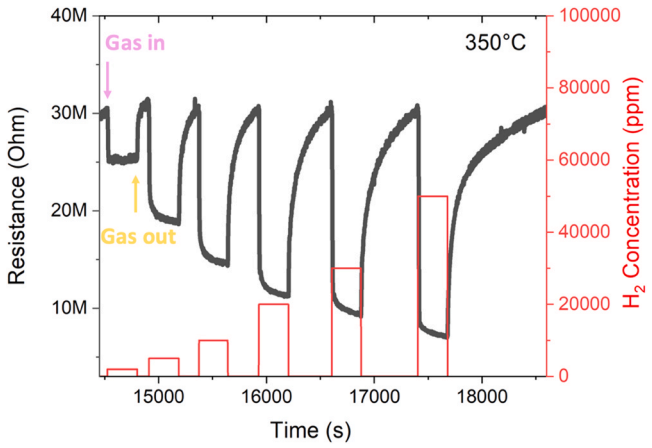

Fig. 2. Dynamic resistance variation of WO_3-based sensor (black curve) at 350 °C under different H_2 concentrations (red curve). Arrows indicate when H_2 is fluxed in the chamber (named "gas in") or it is stopped (named "gas out"). (For interpretation of the references to colour in this figure legend, the reader is referred to the web version of this article.)

operating at 40 kV and 30 mA. The transmittance spectra were obtained by using a UV–VIS–NIR spectrophotometer Varian Cary 500. Gas sensing measurements were performed in a stainless-steel test chamber which allowed measurements in a controlled atmosphere. Gases coming from certified bottles were used and diluted in synthetic dry air at a given concentration by using mass flow controllers. The sensor was heated from room temperature (~20 °C) up to 400 °C under a dry air (RH < 3%) total stream of 100 sccm by using a dual-channel power supplier instrument Agilent E3632A to bias the built-in heater. The response to different gases was evaluated by recording the resistance at an applied voltage of 1.0 V through a Keithley 6487 picometer with a time sensitivity of about 2.5 s. A detailed description of the sensor platform and the setup for H_2 sensing tests are reported in a previous paper [27].

3. Results and discussion

3.1. Structural and electrical properties of WO_3 nanorods

Fig. 1a shows low and high (inset) magnification SEM images of obtained powder on interdigitated electrode, confirming the nanorods morphology. An aspect ratio of about 8 is determined by SEM images showed in Fig. S1 (nanorods average length and diameter of 400 and 50 nm, respectively). All interdigitated fingers were covered to maximize the response during gas sensing measurements. Some drops of WO_3 nanorods solution (powder well dissolved in deionized water) were drop casted on a corner glass and XRD analyses were performed to identify the crystal structure of our nanostructures. From the powder diffraction pattern shown in Fig. 1b, the typical peaks of hexagonal WO_3 (PDF card 00 075 2187) can be observed, with the corresponding Miller Indexes reported. This result confirms the hexagonal structure of WO_3 nanorods.

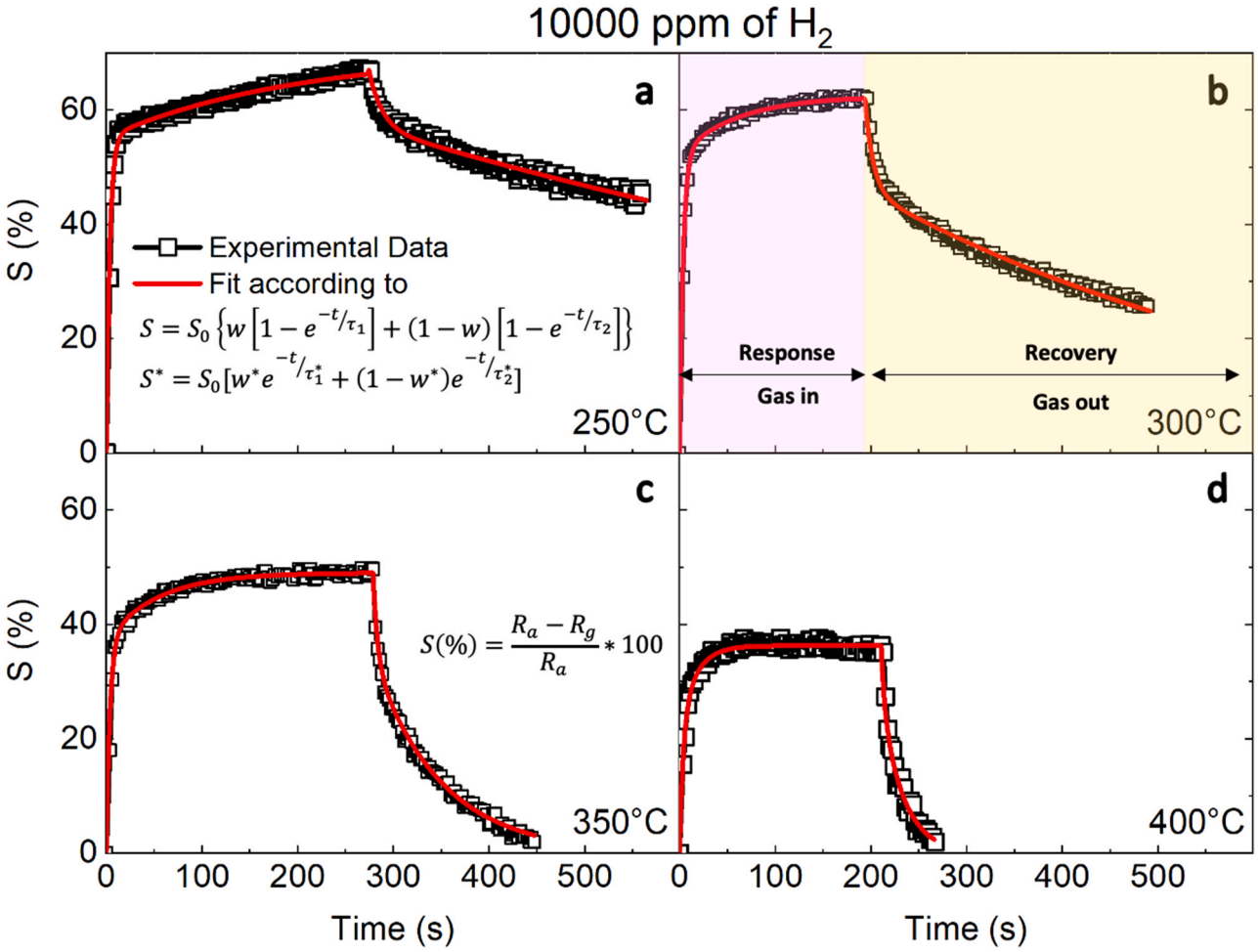

Fig. 3. Dynamic responses of WO_3-based sensor (squared symbols) and fit (red lines) obtained at (a) 250 °C, (b) 300 °C, (d) 350 °C, and (d) 400 °C under 10,000 ppm of H_2 as a function of elapsed time starting when H_2 is fluxed in chamber. (For interpretation of the references to colour in this figure legend, the reader is referred to the web version of this article.)

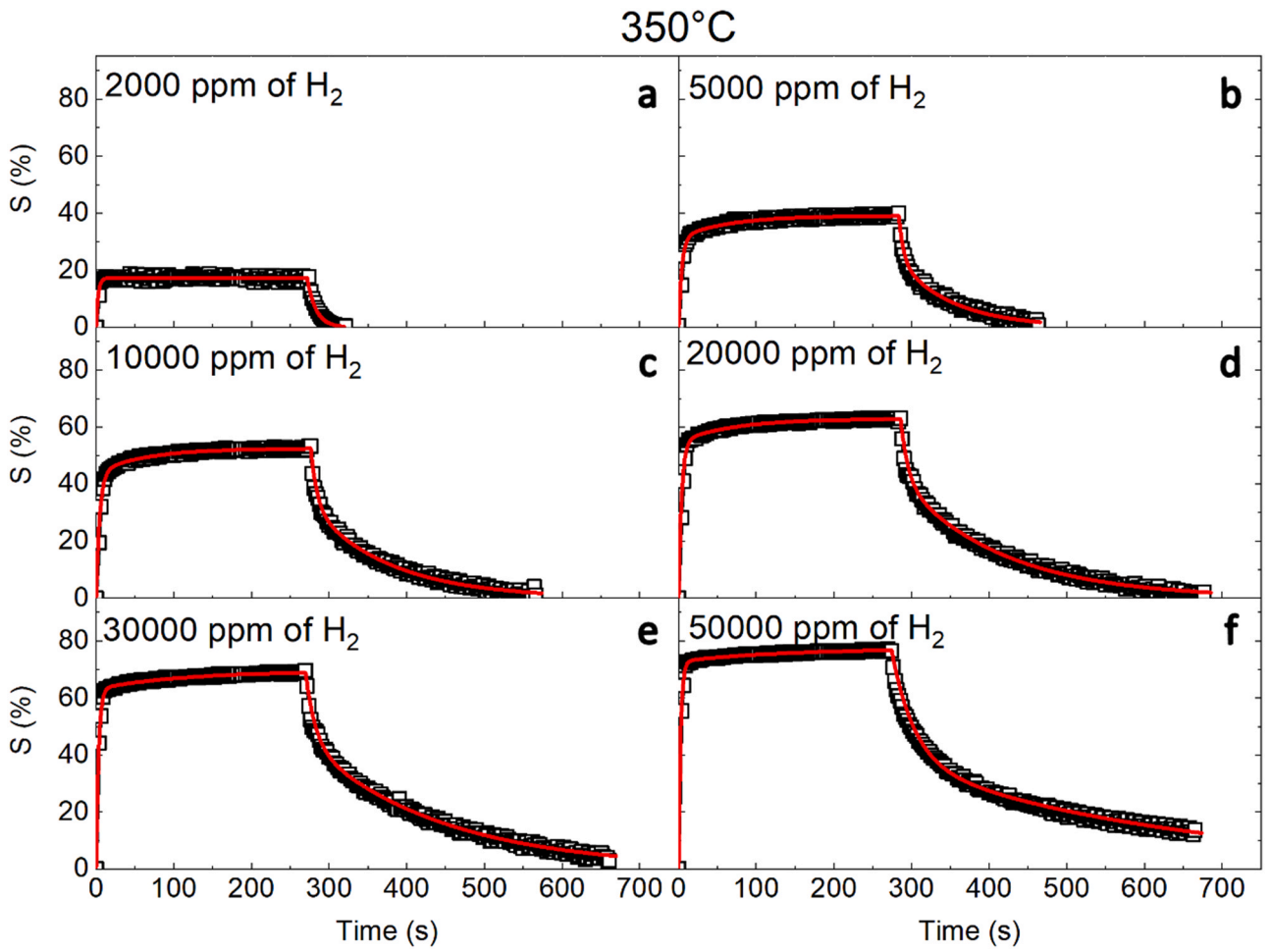

Fig. 4. Dynamic responses of WO_3-based sensor (squared symbols) and fit (red lines) obtained at 350 °C under (a) 2000 ppm, (b) 5000 ppm, (c) 10,000 ppm, (d) 20,000 ppm, (e) 30,000 ppm and (f) 50,000 ppm fluxes of H_2 as a function of elapsed time. (For interpretation of the references to colour in this figure legend, the reader is referred to the web version of this article.)

We investigated the electrical resistance R in dry air at different temperatures T (Fig. 1c). By increasing the temperature from 250° to 400 °C, the electrical conductance G ($=1/R$) of WO_3 nanorods increases by almost three orders of magnitude, following an exponential behavior with an activation energy E_b of 0.53 eV. In an *n*-type semiconductor, as the WO_3, the conductivity depends on electron concentration in conduction band and on electron mobility. Disregarding the thermal dependence of electron mobility, the measured activation energy for conductance could account for the energy position (0.53 eV) below the conduction band of the intrinsic donor-like defects of undoped WO_3, in agreement with Kalanur et al. [28].

3.2. H_2 sensing results

Experimental H_2 sensing curves are obtained by measuring resistance variations as a function of time while a mixture of H_2 and dry air (response phase) or dry air only (recovery phase) are fluxed in the chamber. Resistance variations measured at different temperatures under dry synthetic air and 350 °C under different H_2 concentrations are reported in Fig. S2. To investigate the WO_3-H_2 interaction, we tested different concentrations (2000–50,000 ppm) and different temperatures (250–400 °C). Fig. 2 shows resistance variations (black curve) at 350 °C under different H_2 concentrations (red curve), confirming a strong dependence of resistance on H_2 concentration. Resistance decreases when H_2 is fluxed in the test chamber (gas in arrow), while increases when H_2 flux is stopped (gas out arrow).

From experimental curves of resistance variation, a sensor response *S (%)* can be defined. Since WO_3 is an *n-type* semiconductor and H_2 is a reducing gas, *S (%)* is determined as follows:

$$S(\%) = (R_a - R_g)/R_a * 100 \quad (3.2.1)$$

in which R_g and R_a are the measured resistances in presence and absence of H_2 gas, respectively. To understand WO_3–H_2 interaction, S (%) is defined for each tested temperature and concentration. Fig. 3 shows sensor response curves obtained at each temperature (250–400 °C) as a function of elapsed time during the "response" (pink background in panel b) and "recovery" (yellow background in the panel b) phase, respectively.

In each case of Fig. 3, the response curve increases rapidly when H_2 is fluxed into the chamber, while it tends to saturate after about 20 s. When H_2 flux is stopped, the recovery mechanism starts, and the curves decrease in a temperature dependent way.

H_2 concentration tests are carried out at 350 °C and Fig. 4 shows response and recovery curves obtained under (a) 2000 ppm, (b) 5000 ppm, (c) 10,000 ppm, (d) 20,000 ppm, (e) 30,000 ppm, and (f) 50,000 ppm fluxes of H_2.

Response curves increase rapidly when H_2 gas is fluxed in chamber. After about 20 s the curves tend to saturation and when H_2 flux is stopped the recovery mechanism starts, with the curves decreasing rapidly at first but then slowly tending to the initial value.

About the stability, different pulses of 10,000 ppm of H_2 were fluxed into the chamber at 350 °C, as shown in Fig. S3(a). The sensor response

Table 1
Results of the fitting procedure to response and recovery transients at various temperatures and at fixed concentration of H_2 (10,000 ppm) based on Eqs. (3.3.1) and (3.3.2).

Temperature (°C)	S_0 (%)	τ_1 (s)	τ_2 (s)	w (%)	τ^*_1 (s)	$\tau*2$ (s)	w^* (%)
250	70	4	200	78	14	1137	15
300	63	4	61	83	8	483	29
350	49	4	54	76	5	71	32
400	36	4	16	60	3	23	25

Table 2
Results of the fitting procedure to response and recovery transients at various concentrations of H_2 at a temperature of 350 °C, based on Eqs. (3.3.1) and (3.3.2).

Concentration 10^3 (ppm)	S_0 (%)	τ_1 (s)	τ_2 (s)	w (%)	τ^*_1 (s)	$\tau*2$ (s)	w^* (%)
2	17	3	–	100	11	–	100
5	39	4	63	80	6	71	42
10	53	5	65	84	8	102	40
20	63	4	70	87	10	132	34
30	69	3	111	91	12	174	36
50	77	3	126	94	29	359	50

shows a slight drift after 4 pulses, demonstrating a fair stability and a good reactivation, since the resistance is restored at the initial condition. Moreover, we tested WO_3 sensor selectivity under pulses of different gases (10,000 ppm of H_2, 500 ppm of NO and 50 ppm of CO) at temperatures ranging between 250 ° and 400 °C as shown in Fig. S3(b). The H_2 response is higher than the NO response, especially at higher temperatures, while no response is obtained for CO whatever the temperature is, confirming a certain selectivity of the WO_3 sensor towards H_2 as previously reported in the literature [7]. The calibration curve at 350 °C is reported in Fig. S3(c). The LoD (Limit of Detection), calculating by considering S/N = 3, is 1076 ppm [29].

3.3. H_2 sensing kinetics

To determine the kinetics of the H_2 sensing, all experimental response curves were fitted by considering the Langmuir absorption theory with two isotherms (two processes are assumed to play independent roles). According to Langmuir, sensor response during the "gas in" phase, S, and during the "gas out" phase, S^*, can be fitted as follows [29]:

$$S = S_0\{w[1-\exp(-t/\tau_1)] + (1-w)[1-\exp(-t/\tau_2)]\} \quad (3.3.1)$$

$$S^* = S_0[w^* * \exp(-t/\tau_1^*) + (1-w^*) * \exp(-t/\tau_2^*)] \quad (3.3.2)$$

in which S_0 is the maximum value of resistance change (the same value was fixed for response and recovery phases), τ_n and τ_n^* (n stands for 1 or 2) are lifetimes associated to the two isotherms during response and recovery phases, respectively; w and w^* are weights attributed to process 1 during response and recovery phases, respectively.

The fitting curves (red lines) shown in Fig. 3 are in excellent agreement with experimental data (black squares), supporting the hypothesis of a fast (P1) and a slow (P2) process, independent and concomitant. The fitting parameters are listed in Table 1.

The maximum response value (S_0) changes with temperature: it is maximum (70 %) at 250 °C, as expected given the very high resistance at this temperature. Lifetimes and weights are reported in Fig. S4 as a function of temperature. P1 is characterized by times of few seconds (roughly the time resolution of experimental set-up), both in response and in recovery phases and regardless of temperature, while P2 is characterized by long times (10–200 s) in response and (20–1100 s) in recovery phases. In both cases, τ_2 and τ_2^* are clearly dependent on

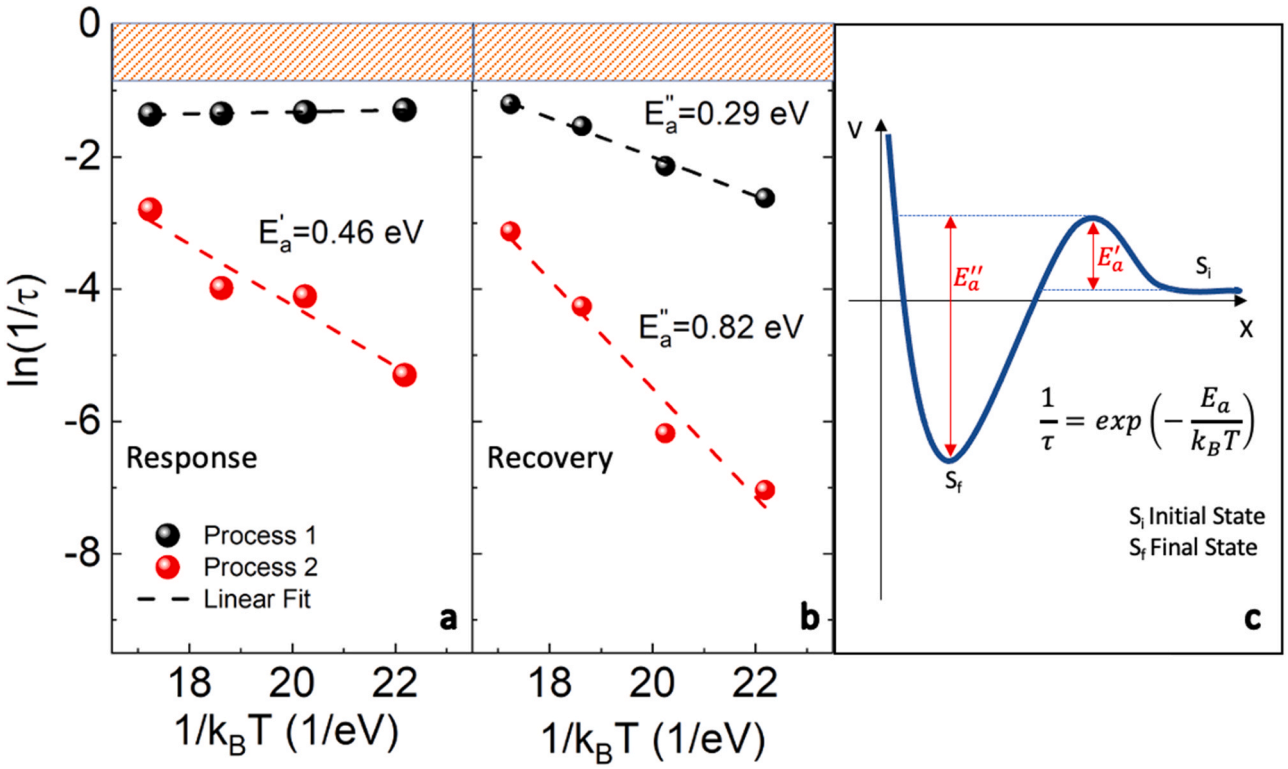

Fig. 5. Arrhenius plot of inverse of lifetime τ of P1 (black sphere) and P2 (red sphere) during (a) response and (b) recovery phase. Dotted lines are linear fit to each set of data. The evidenced region indicates the time resolution of experimental set-up. (c) schematic representation of energy barriers for the sensing processes. (For interpretation of the references to colour in this figure legend, the reader is referred to the web version of this article.)

temperature, since they decrease when temperature increases. Concerning the weight, *w*, P1 is predominant (*w* around 60–84%) during the response phase while it is minority during the recovery phase. Such a result could suggest different mechanisms occurring during response and recovery phases.

We performed an analogous analysis when tests were carried out at fixed temperature by varying H_2 concentration. For all these cases shown in Fig. 4, except at 2000 ppm, Eqs. (3.3.1) and (3.3.2) can be used to fit experimental curves by obtaining good agreement. In the case of the lowest concentration (Fig. 4(a)) only one process (P1) is identified both during the response and the recovery phase, and so, *w* is maximum. Table 2 reports all parameters obtained from fitted curves. The maximum response values depend on concentration since the highest value (77%) is obtained at a higher concentration (50,000 ppm). Moreover, lifetimes and weights are reported in Fig. S5 as a function of concentration.

Both in response and recovery phases, P1 is characterized by short lifetimes, regardless of concentration, while P2 has increasing lifetimes with increasing concentration. P1 is predominant in the response phase since *w* is around 80–95%, but not during the recovery phase. Also, in this case, this can be due to different mechanisms occurring during response and recovery phases. Fig. S4(a) shows the *w* trend as a function of H_2 concentration in cases where 2 processes are identified, revealing an exponentially increasing trend up to saturation. It should be noted that, within the Langmuir theory, the surface coverage θ_m by the adsorbed gas molecules [30] is expected to increase similarly. This evidence suggests that process P1 is related to a surface coverage by H_2.

The Langmuir adsorption model with two isotherms very well describes our experimental data, pointing out that the WO_3-H_2 interaction proceeds through at least two ways. Indeed, the thermal dependence of τ is highly significant as it will unveil the energy barrier for concurring processes. Fig. 5 reports the inverse of lifetimes for the two processes, both in response (a) and in recovery (b) phases in an Arrhenius plot, by clearly showing linear behaviors for the four cases. It should be noted that in the response phase the fast process is too close to the time resolution which hinders us to resolve high frequency (orange box in Fig. 5) so that the linear trend can be meaningfulness only for this process. The inverse of a lifetime gives the probability rate, which is thermally activated, as follows:

$$1/\tau = exp(-E_a/k_BT) \quad (3.2.3)$$

where k_B is Boltzmann constant, T is temperature and E_a is activation energy (E_a' for response phase and E_a'' for recovery phase). The physical meaning of these activation energies is depicted in Fig. 5c, as kinetic energy barriers in the interaction potential V between the WO_3 surface and the approaching H_2 molecule. By analyzing the meaningful Arrhenius plots reported in Fig. 5 for P1 (black spheres) and P2 (red spheres) involved during (a) response phase and (b) recovery phase, we can extract E_a values for each involved process (dotted lines). The result of such an exercise gives E_a of 461 meV in the response phase for P2; 295 meV and 821 meV in the recovery phase for P1 and P2, respectively. The experimental determination of these activation energies is a key point to reach a solid description of the WO_3-H_2 interaction leading to H_2 sensing.

3.4. Modeling of WO_3-H_2 interaction

It is well assessed that H intercalation occurs in hexagonal WO_3, especially during the electrochromic process [31]. H_2 intercalation causes internal changes of WO_3 structure also reflected by a significant change of optical transmittance. Mattoni et al., proposed that WO_3-H_2 interaction leads to H_2 intercalation in WO_3 crystals [17], while for other models such a process is not required. It is essential now to prove if H_2 intercalation occurs or not in our samples. To this aim, several drops of WO_3 nanorods solution were dropped on corning glass substrates,

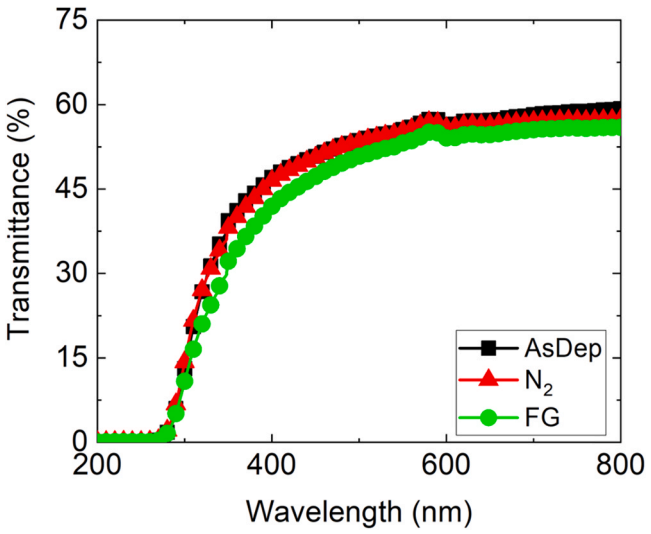

Fig. 6. Transmittance spectra of AsDep (black line + squares), N_2 (red line + triangles), and FG (green line + circles) samples. (For interpretation of the references to colour in this figure legend, the reader is referred to the web version of this article.)

realizing a very thin film. Two WO_3 coated glasses were annealed at 350 °C for 30 min in forming gas (*FG*, gas mixture of N_2:H_2 =95:5) or in N_2. Annealing in FG simulates the exposure of WO_3 nanorods to H_2 gas during the sensing test at 350 °C. Transmittance spectra acquired just after annealing of WO_3 coated glasses are shown in Fig. 6. The annealing in inert ambient does not significantly modify the transmittance curve of the sample. FG annealing induces a barely appreciable reduction of transmittance, far away from the expected chromism induced by intercalating H_2. Moreover, the H_2 intercalation typically produces an enhancement in measured resistance according to Mirzaei et al. [32] as following reaction consequence:

$$xH^+ + xe^- + WO_3 \rightarrow H_xWO_3$$

On the contrary, after H_2 exposure, our samples reveal a marked decreased resistance at any temperature and any H_2 concentration. Such evidence, together with transmittance spectra, tell us that during H_2 exposure H intercalation in WO_3 nanorods, if any, is not a key process and can be ruled out in modeling the WO_3-H_2 interaction.

To model the WO_3-H_2 interaction, we now need to discuss the P1 and P2 occurring in response and recovery phase. Firstly, it must be specified that during the response phase the interaction will involve H_2, while during the recovery phase, only residual H_2, if any, can be considered. Experimental results give us much information about active processes. The evidence can be summarized as follows: (i) P1 is faster than P2, both in response and in recovery phases. τ_1 is around 4 s, regardless of temperature and concentration, while τ_1^* slightly depends on temperature and concentration; (ii) P1 is more probable than P2, both in response and recovery phases, and at any temperature and any concentration; (iii) the H_2 concentration dependence of *w* suggests a surface process for P1; (iv) Arrhenius plots hint that P1 is a very fast process in response phase, while it is thermally activated (E''_a=295 meV) at recovery phase when the temperature is ranging between 250 °C and 400 °C. P2 needs high activation energy both in response (461 meV) and recovery phases (821 meV) in the same temperature range; (v) at very low H_2 concentration (below 5000 ppm), only one process is active.

Considering the above discussion on experimental evidence, and assuming that WO_3 nanorods are typically adsorbed with oxygen at surface, the following model is proposed. In response phase, P1 can be described as a *surface process* where a spontaneous interaction occurs between H_2 molecules and oxygen ions adsorbed on the WO_3 surface leading to a water molecule as follows:

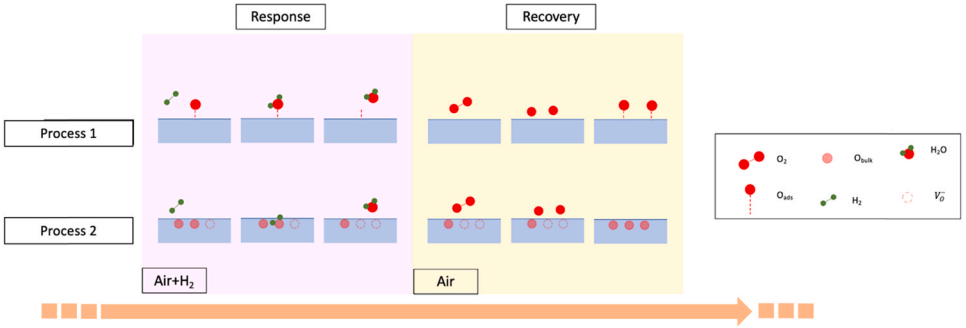

Fig. 7. Schematic model of surface processes (P1) and bulk processes (P2) involved during the response (pink evinced area) and the recovery (yellow evidenced area) phase. H_2 interacts with adsorbed oxygen and oxygen directly bound to W to produce a water molecule in response phase, while O_2 can be adsorbed on WO_3 surface or can occupy oxygen vacancy for restoring the initial condition. (For interpretation of the references to colour in this figure legend, the reader is referred to the web version of this article.)

$$H_2 + O^{2-}_{ads} \text{ -> } H_2O + 2e'$$

In addition, once water evaporated and oxygen adsorbed on the surface has been reduced, H_2 interacts with the bare WO_3 surface through a *bulk process* involving oxygen atoms bound to surface W atoms [33]. This interaction can lead to P2 in response phase when a water molecule is produced leaving an oxygen vacancy $V_O^{\cdot\cdot}$, as follows:

$$H_2 + O_{bound} \text{ -> } H_2O + 2e' + V_O^{\cdot\cdot}$$

During response phase, both P2 and P1 produce a decrease in measured resistance, according to experimental data.

A different scenario occurs in the recovery phase, where the most probable interaction occurs between O_2 present in dry synthetic air and WO_3 surface. P1 can arise from interaction with oxygen adsorbed on WO_3 surfaces, depending on working temperature as follows [23]:

$$O_{2(gas)} \rightarrow O_{2(ads)}$$

$$O_{2(ads)} + e' \rightarrow O^-_{2(ads)} \text{ if } T < 100\ ^\circ C$$

$$O^-_{2(ads)} + e' \rightarrow 2O^-_{(ads)} \text{ if } 100\ ^\circ C < T < 300\ ^\circ C$$

$$O^-_{(ads)} + e' \rightarrow O^{2-}_{(ads)} \text{ if } T > 300\ ^\circ C$$

P2 can be described as the interaction among O_2 and oxygen vacancies, leading to defect recombination as follows:

$$O_2 + V_O^{\cdot\cdot} + 2\ e' \rightarrow O_{bound}$$

Processes occurring in the recovery phase let WO_3 resistance increase, according to experimental data. At very low H_2 concentration, only surface processes occur, both in response and recovery phases. The H_2-WO_3 interaction, under exposure to high H_2 concentration, could produce a so high density of oxygen vacancies at surface that a diffusion towards bulk can occur. Such a scenario could explain the long response and recovery times at high H_2 concentration (Table 2).

Fig. 7 shows a schematic representation of the above-proposed model during response and recovery phases (pink and yellow evidenced area, respectively), where the distinction between *surface* and *bulk process* (P1 and P2 respectively) is clear.

4. Conclusion

We investigated WO_3-H_2 interaction by testing WO_3 nanorods exposed to H_2 (2000–50,000 ppm) fluxes at different temperatures (250–400 °C). The Langmuir adsorption theory was successfully used to model experimental data of sensing kinetics, evidencing that two processes occur both in response and in recovery phases, regardless of the temperature, for concentrations larger than 5000 ppm. The fast process (lifetimes of few seconds) is attributed to H_2 interaction with adsorbed O at WO_3 surface, in the response phase, and to O adsorption (barrier of 0.29 eV), in the recovery phase. Since a high concentration of H_2 consumes all adsorbed oxygen leaving WO_3 uncovered, the slow process (lifetimes of hundreds of seconds) is attributed to generation (barrier of 0.46 eV) and recombination (barrier of 0.82 eV) of oxygen vacancies in WO_3 nanorods. No H intercalation in WO_3 bulk is observed. At low H_2 concentrations, only fast processes are evidenced, which are linked to surface processes. Our data and modeling show that WO_3 nanorods are a promising material for H_2 sensing and, to improve the sensitivity at low hydrogen concentrations, increasing the exposed surface of WO_3 nanorods is beneficial for fast detection.

Funding

This work was supported by programma ricerca di Ateneo UNICT 2020-22 linea 2 PIA.CE.RI "NaTI4Smart Sviluppo di NAnomateriali e Tecnologie Innovative per Smart detection", by PRIN 2017 "CLEAN-Valorizing Sustainable Plastics through a CLEver use of NANoparticles" 20174FSRZS_003 and by "PON MIUR ADAS +" (ARS01_00459).

CRediT authorship contribution statement

G. Mineo, S. Mirabella, E. Bruno: conceptualization; **G. Mineo, K. Moulaee, G. Neri, S. Mirabella, E. Bruno**: investigation; **G. Mineo, K. Moulaee, G. Neri, S. Mirabella, E. Bruno:** methodology; **G. Neri, S. Mirabella, E. Bruno:** supervision; **G. Mineo:** writing—original draft; **G. Mineo, G. Neri, S. Mirabella, E. Bruno:** writing—review and editing. All authors have read and agreed to the published version of the manuscript.

Declaration of Competing Interest

The authors declare that they have no known competing financial interests or personal relationships that could have appeared to influence the work reported in this paper.

Acknowledgements

The authors wish to thank G. Malandrino (University of Catania, Italy) for useful discussions and experimental XRD contribution, G. Pantè, C. Percolla and S. Tatì (CNR-IMM Catania, Italy) for technical support and the Service Center B.R.I.T. of University of Catania.

Appendix A. Supporting information

Supplementary data associated with this article can be found in the online version at doi:10.1016/j.snb.2021.130704.

References

[1] J. Yang, A. Sudik, C. Wolverton, D.J. Siegel, High capacity hydrogen storage materials: attributes for automotive applications and techniques for materials discovery, Chem. Soc. Rev. 39 (2) (2010) 656–675, https://doi.org/10.1039/B802882F.

[2] H. Zhao, D. Lu, J. Wang, W. Tu, D. Wu, S.W. Koh, P. Gao, Z.J. Xu, S. Deng, Y. Zhou, B. You, H. Li, Raw biomass electroreforming coupled to green hydrogen

generation, Nat. Commun. 12 (2021) 1–10, https://doi.org/10.1038/s41467-021-22250-9.
[3] Ohsawa, M. Ishikawa, K. Takahashi, M. Watanabe, K. Nishimaki, K. Yamagata, K. I. Katsura, Y. Katayama, S. Asoh, S. Ohta, Hydrogen acts as a therapeutic antioxidant by selectively reducing cytotoxic oxygen radicals, Nat. Med. 13 (2007) 688–694, https://doi.org/10.1038/nm1577.
[4] T. Hübert, L. Boon-Brett, G. Black, U. Banach, Hydrogen sensors—A review, Sens. Actuators, B Chem. 157 (2011) 329–352, https://doi.org/10.1016/j.snb.2011.04.070.
[5] Y. Luo, C. Zhang, B. Zheng, X. Geng, M. Debliquy, Hydrogen sensors based on noble metal doped metal-oxide semiconductor: a review, Int. J. Hydrog. Energy 42 (2017) 20386–20397, https://doi.org/10.1016/j.ijhydene.2017.06.066.
[6] H. Zheng, J.Z. Ou, M.S. Strano, R.B. Kaner, A. Mitchell, K. Kalantar-Zadeh, Nanostructured tungsten oxide - properties, synthesis, and applications, Adv. Funct. Mater. 21 (2011) 2175–2196, https://doi.org/10.1002/adfm.201002477.
[7] S.K. Deb, Opportunities and challenges in science and technology of WO_3 for electrochromic and related applications, Sol. Energy Mater. Sol. Cells 92 (2008) 245–258, https://doi.org/10.1016/j.solmat.2007.01.026.
[8] J. Shi, Z. Cheng, L. Gao, Y. Zhang, J. Xu, H. Zhao, Facile synthesis of reduced graphene oxide/hexagonal WO_3 nanosheets composites with enhanced H_2S sensing properties, Sens. Actuators, B Chem. 230 (2016) 736–745, https://doi.org/10.1016/j.snb.2016.02.134.
[9] H. Ji, W. Zeng, Y. Xu, Y. Li, Nanosheet-assembled hierarchical WO] flower-like nanostructures: hydrothermal synthesis and NH_3-sensing properties, Mater. Lett. 250 (2019) 155–158, https://doi.org/10.1016/j.matlet.2019.05.023.
[10] Z. Hua, C. Tian, Z. Qiu, Y. Li, X. Tian, M. Wang, E. Li, An investigation on NO_2 sensing mechanism and shielding behavior of WO_3 nanosheets, Sens. Actuators, B Chem. 259 (2018) 250–257, https://doi.org/10.1016/j.snb.2017.12.016.
[11] Y. Zhang, W. Zeng, Y. Li, NO_2 and H_2 sensing properties for urchin-like hexagonal WO_3 based on experimental and first-principle investigations, Ceram. Int. 45 (2019) 6043–6050, https://doi.org/10.1016/j.ceramint.2018.12.075.
[12] F. Zheng, C. Xi, J. Xu, Y. Yu, W. Yang, P. Hu, Y. Li, Q. Zhen, S. Bashir, J.L. Liu, Facile preparation of WO_3 nano-fibers with super large aspect ratio for high performance supercapacitor, J. Alloy. Compd. 772 (2019) 933–942, https://doi.org/10.1016/j.jallcom.2018.09.085.
[13] P.A. Shinde, A.C. Lokhande, A.M. Patil, C.D. Lokhande, Facile synthesis of self-assembled WO_3 nanorods for high-performance electrochemical capacitor, J. Alloy. Compd. 770 (2019) 1130–1137, https://doi.org/10.1016/j.jallcom.2018.08.194.
[14] J. Zhang, X. Liu, G. Neri, N. Pinna, Nanostructured materials for room-temperature gas sensors, Adv. Mater. 28 (2016) 795–831, https://doi.org/10.1002/adma.201503825.
[15] P.S. Kolhe, P. Mutadak, N. Maiti, K.M. Sonawane, Synthesis of WO_3 nanoflakes by hydrothermal route and its gas sensing application, Sens. Actuators A: Phys. 304 (2020), 111877, https://doi.org/10.1016/j.sna.2020.111877.
[16] S.H. Lee, R. Deshpande, P.A. Parilla, K.M. Jones, B. To, A.H. Mahan, A.C. Dillon, Crystalline WO_3 nanoparticles for highly improved electrochromic applications, Adv. Mater. 18 (2006) 763–766, https://doi.org/10.1002/adma.200501953.
[17] G. Mattoni, B. De Jong, N. Manca, M. Tomellini, A.D. Caviglia, Single-crystal Pt-decorated WO_3 ultrathin films: a platform for sub-ppm hydrogen sensing at room temperature, ACS Appl. Nano Mater. 1 (2018) 3446–3452, https://doi.org/10.1021/acsanm.8b00627.
[18] C.H. Wu, Z. Zhu, S.Y. Huang, R.J. Wu, Preparation of palladium-doped mesoporous WO_3 for hydrogen gas sensors, J. Alloy. Compd. 776 (2019) 965–973, https://doi.org/10.1016/j.jallcom.2018.10.372.
[19] S. Zeb, G. Sun, Y. Nie, Y. Cui, X. Jiang, Synthesis of highly oriented WO_3 nanowire bundles decorated with Au for gas sensing application, Sens. Actuators B: Chem. 321 (2020), 128439, https://doi.org/10.1016/j.snb.2020.128439.
[20] F. Zheng, L. Zhang, Y.Y. Li, Q. Liu, Z. Li, H.C. Yao, Bimetallic AuPd alloy nanoparticles decorated on macroporous WO_3 supports for selective detection of acetone, ACS Appl. Nano Mater. (2021) 4–11, https://doi.org/10.1021/acsanm.0c03345.
[21] S. Kim, S. Park, S. Park, C. Lee, Acetone sensing of Au and Pd-decorated WO_3 nanorod sensors, Sens. Actuators, B Chem. 209 (2015) 180–185, https://doi.org/10.1016/j.snb.2014.11.106.
[22] Zaleska-Medynska, M. Marchelek, M. Diak, E. Grabowska, Noble metal-based bimetallic nanoparticles: the effect of the structure on the optical, catalytic and photocatalytic properties, Adv. Colloid Interface Sci. 229 (2016) 80–107, https://doi.org/10.1016/j.cis.2015.12.008.
[23] C.H. Chang, T.C. Chou, W.C. Chen, J.S. Niu, K.W. Lin, S.Y. Cheng, J.H. Tsai, W. C. Liu, Study of a WO_3 thin film based hydrogen gas sensor decorated with platinum nanoparticles, Sens. Actuators B: Chem. 317 (2020), 128145, https://doi.org/10.1016/j.snb.2020.128145.
[24] F.H. Tian, C. Gong, Y. Peng, X. Xue, H_2 sensing mechanism under different oxygen concentration on the hexagonal WO_3 (001) surface: a density functional theory study, Sens. Actuators, B Chem. 244 (2017) 655–663, https://doi.org/10.1016/j.snb.2016.12.035.
[25] J. Wang, E. Khoo, P.S. Lee, J. Ma, Controlled synthesis of WO_3 nanorods and their electrochromic properties in H_2SO_4 electrolyte, J. Phys. Chem. C. 113 (2009) 9655–9658, https://doi.org/10.1021/jp901650v.
[26] T. Peng, D. Ke, J. Xiao, L. Wang, J. Hu, L. Zan, Hexagonal phase WO_3 nanorods: hydrothermal preparation, formation mechanism and its photocatalytic O_2 production under visible-light irradiation, J. Solid State Chem. 194 (2012) 250–256, https://doi.org/10.1016/j.jssc.2012.05.016.
[27] Gullino, M. Parvis, L. Lombardo, S. Grassini, N. Donato, K. Moulaee, G. Neri, Employment of Nb2O5 thin-films for ethanol sensing, in Proc. IEEE International Instrumentation and Measurement Technology Conference (I2MTC), 2020 1–6. https://doi.org/10.1109/I2MTC43012.2020.9128457.
[28] S.S. Kalanur, Structural, optical, band edge and enhanced photoelectrochemical water splitting properties of Tin-doped WO_3, Catalysts 9 (2019) 456, https://doi.org/10.3390/catal9050456.
[29] M. Urso, S.G. Leonardi, G. Neri, S. Petralia, S. Conoci, F. Priolo, S. Mirabella, Room temperature detection and modelling of sub-ppm NO_2 by low-cost nanoporous NiO film, Sens. Actuators B: Chem. 305 (2020), 127481, https://doi.org/10.1016/j.snb.2019.127481.
[30] K. Mukherjee, S.B. Majumder, Analyses of response and recovery kinetics of zinc ferrite as hydrogen gas sensor, J. Appl. Phys. 106 (2009), 064912, https://doi.org/10.1063/1.3225996.
[31] K. Bange, Colouration of tungsten oxide films: a model for optically active coatings, Sol. Energy Mater. Sol. Cells 58 (1) (1999) 1–131.
[32] A. Mirzaei, J.H. Kim, H.W. Kim, S.S. Kim, Gasochromic WO_3 nanostructures for the detection of hydrogen gas: an overview, Appl. Sci. 9 (2019) 1775, https://doi.org/10.3390/app9091775.
[33] A. Georg, W. Graf, R. Neumann, V. Wittwer, Mechanism of the gasochromic coloration of porous WO_3 films, Solid State Ion. 127 (2000) 319–328, https://doi.org/10.1016/S0167-2738(99)00273-8.

Giacometta Mineo attained the master degree in physics at the University of Catania (Italy) in October 2019. Currently, she is a second year Ph.D. student in Materials Science and Nanotechnologies. Her experimental research activity concerns the low-cost synthesis of WO_3-based nanostructures and their physical-chemical characterization for sensing and energy storage applications.

Kaveh Moulaee received his B.Sc. in pure chemistry in 2009 from Department of Chemistry of the Isfahan University, Isfahan, Iran and his M.Sc. in analytical chemistry in 2011 from Shahid Chamran University, Ahvaz, Iran. Currently, he is pursuing PhD under the University of Messina, Italy. His main research interests are electroanalytical chemistry, electrocatalysis, nanochemistry and gas sensors

Giovanni Neri received a degree in Chemistry in 1980. Since 2001 he has been a Full Professor of Chemistry at the University of Messina. He spent several periods as visiting professor at the University of Michigan (USA), University of Alagappa and Indian Institute of Technology Indore (INDIA). From 2004–2007, he was the Director of the Department of Industrial Chemistry and Materials Engineering at the University of Messina. In 2013 he has been awarded with a grant by Samsung SAIT Global Research Outreach program for the project “Smart sensors for breath analysis”. His research activities cover many aspects of the synthesis and characterization of materials and the study of their sensing properties. His recent research has been focused on the application of gas sensors composed of nanostructured metal oxides and novel organic–inorganic hybrid nanocomposites and enzyme-free electrochemical sensors. Prof. Neri is author of more than 300 scientific publications in international journals. The number of citations as reported in Scopus is more than 8300, with an h-index of 49.

Salvo Mirabella is an Associate Professor in Experimental Condensed Matter Physics at the University of Catania (since 2016). He received his Laurea (1999) and PhD (2003) in Physics from the University of Catania (Italy). His research activity is mainly experimental, focusing on semiconductor nanostructures for Smart Sensing, Photovoltaics, Microelectronics. Since 2000 Salvo contributed to more than 150 papers, holding a H- factor 31. His outreach activity goes from local actions (aimed at high school students) to national and international events such as FameLab, Pint of Science, European Researcher’s Night.

Elena Bruno is an Associate Professor permanent employed at the Department of Physics and Astronomy, University of Catania since 31/12/2010. She deals with experimental research on the synthesis of materials and nanostructures for micro and optoelectronics, sensors, energy and water treatment.